

Verification of a Boundary Element Model for Wave Forces on Structures with Porous Elements

E.B.L. Mackay, A. Feichtner, R.E. Smith, P.R. Thies, & L. Johanning

University of Exeter, College of Engineering Mathematics & Physical Sciences, Penryn, TR10 9FE, UK

ABSTRACT: Hydrodynamic parameters on structures with porous elements can be significantly altered compared to those on solid structures. The use of a porous support structure for a floating wind turbine could potentially reduce platform motions and wave forces, correspondingly reducing adverse effects on the wind turbine, such as fatigue damage and loss in energy capture. This paper presents a boundary element method (BEM) to calculate linear wave forces on solid structures with a porous wall bounding an interior volume of water. In the model, the shape of the solid and porous elements of the structure can take arbitrary shapes and be either surface-piercing or fully submerged. Initial verification results are presented against existing commercial BEM software for solid bodies and analytical results for solid/porous structures with simple geometries. In all cases, the comparisons show good agreement, giving confidence that the method can be used in more complex cases where analytical results cannot be derived.

1 INTRODUCTION

Wave interaction with porous structures have been studied in a range of applications in coastal and offshore engineering. The primary purpose of introducing porous elements in an offshore structure is to dissipate wave energy, analogous to the use of porous wave absorbers in narrow wave flumes in the form of foam or wire meshes. Porous elements in offshore structures tend to be thin in comparison to the wavelength, comprising a thin perforated or slatted sheet. The sharp edges of the perforations cause flow separation and dissipation of energy in turbulent eddies.

Methods for computing wave forces on porous structures have been derived in the context of breakwaters (see Huang et al, 2011, for a review of the wide literature on this topic), gravity bases for offshore wind turbines (Park et al, 2014), motion damping on floating structures (e.g. Downie et al, 2000; Williams et al, 2000; Lee & Ker, 2002; Molin 2011), aquaculture (e.g. Zhao et al., 2010; Dokken et al. 2017) and tuned liquid dampers (e.g. Faltinsen et al, 2011; Crowley & Porter, 2012; Molin & Remy, 2013, 2015). To date, most published work on wave interaction with 3D structures with porous elements has focused on simple geometries, for which analytical solutions can be derived (e.g. Wang & Ren, 1994; Williams & Li, 1998, 2000; Williams et al, 2000; Zhao et al, 2010; Ning et al., 2017). The boundary element method (BEM) has been used in several studies to compute wave forces on 2D porous structures with more complex geometries (e.g. Ijima et al, 1976;

Sulisz, 1985; Mallayachari & Sundar, 1994; Cho & Kim, 2008; Liu et al, 2012; Liu & Li, 2017). Feng et al. (2017) proposed a method for introducing dissipation surfaces (which act in a similar way to porous elements) into a 3D BEM model and applied the model to study gap resonance between side-by-side barges. Dokken et al. (2017) presented a BEM solution for 3D porous structures, with the restriction that the surface of the structure is entirely porous and there are no solid elements.

In the present paper the multi-domain BEM approach of Dokken et al. (2017) is extended to bodies composed of solid parts and porous walls enclosing internal volumes of water. The method presented allows the calculation of wave forces on combined solid-porous structures of arbitrary shape, which cannot be calculated analytically. The present solution differs from that presented by Feng et al. (2017), in that it does not require the calculation of the second derivative of the Green function. The solution of Feng et al. (2017) is a single-domain approach and therefore cannot model the case where a porous wall encloses a volume of water.

The main objective of the present paper is to present the verification of the new BEM model against published results, rather than to study the behaviour of porous structures in detail. The application of the BEM model to study the performance of porous floating platforms for offshore wind turbines will be reported in future work.

2 FORMULATION

The structure is assumed to consist of a single solid body and a porous wall bounding a volume of water connected to this body. The geometry of the solid body and porous wall are arbitrary and may be either submerged or surface-piercing. The surface of the solid body is divided into two parts, an exterior solid surface, S_E , and an interior solid surface, S_I . The porous surface is denoted S_P . The normal vectors to the body surfaces are defined to point out of the fluid domain on the exterior of the porous wall and into the fluid domain on the interior of the porous wall, so that the same normal vectors are used on the porous wall for both the exterior and interior problems. A sketch of the setup and notation is shown in Figure 1, which shows a truncated cylinder with a solid inner column and porous outer wall (a 3D mesh of this geometry is also shown in Figure 10). The coordinate system is defined with $z = 0$ on the free surface and $z = -h$ on the sea bed (in the case of finite depth).

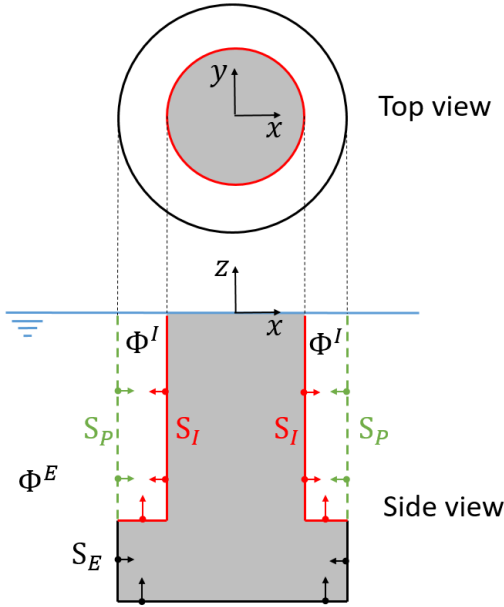


Figure 1. Sketch of definition of surfaces, normal vectors and internal and external fluid domains.

The fluid is assumed to be inviscid and incompressible, and its motion is irrotational, so that a velocity potential can be used to describe the fluid motion. The fluid domain is divided into regions external and internal to the structure, with the potentials in the exterior and interior domains denoted Φ^E and Φ^I . The structure is subject to regular linear waves of amplitude A and angular frequency ω , propagating in a direction at an angle β to the positive x -axis (i.e. $\beta = 0$ corresponds to waves propagating from negative to positive x). The structure is assumed to make 6DOF harmonic motions of amplitude ξ_j , $j = 1, \dots, 6$, corresponding to surge, sway, heave, roll, pitch and yaw. Under these assumptions the potentials in each domain can be written as

$$\Phi^{E,I}(\mathbf{x}, t) = \text{Re} \left\{ e^{i\omega t} \left[\frac{igA}{\omega} [\phi_0(\mathbf{x}) + \phi_7^{E,I}(\mathbf{x})] + i\omega \sum_{j=1}^6 \xi_j \phi_j^{E,I}(\mathbf{x}) \right] \right\}, \quad (1)$$

where g is the acceleration due to gravity, $\mathbf{x} = (x, y, z)$ is the position vector, ϕ_0 is the spatial component of the incident wave potential, $\phi_7^{E,I}$ is the spatial component of the scattering potential and $\phi_j^{E,I}$ ($j = 1, \dots, 6$) are the spatial components of the radiation potentials. The spatial potentials in each domain satisfy the Laplace equation, the linearised free-surface condition and the no-flow condition on the seabed:

$$\nabla^2 \phi_j^{E,I} = 0, \quad j = 0, \dots, 7 \quad (2)$$

$$\frac{\partial \phi_j^{E,I}}{\partial z} = \frac{\omega^2}{g} \phi_j^{E,I} \quad \text{on } z = 0, \quad j = 0, \dots, 7 \quad (3)$$

$$\frac{\partial \phi_j^{E,I}}{\partial z} = 0 \quad \text{on } z = -h, \quad j = 0, \dots, 7 \quad (4)$$

The incident wave potential is given by

$$\phi_0 = D(z) \exp(-ik(x \cos \beta + y \sin \beta)), \quad (5)$$

where k is the wave number, defined as the positive real solution of

$$\omega^2 = kg \tanh(kh), \quad (6)$$

and

$$D(z) = \begin{cases} \exp(kz) & \text{in deep water,} \\ \frac{\cosh(k(z+h))}{\cosh(kh)} & \text{in finite depth.} \end{cases} \quad (7)$$

The radiated and scattered potentials in the exterior domain satisfy a radiation condition in the far-field:

$$\lim_{r \rightarrow \infty} \sqrt{R} \left(\frac{\partial \phi_j^E}{\partial r} + ik \phi_j^E \right) = 0, \quad j = 1, \dots, 7 \quad (8)$$

where $R = \sqrt{x^2 + y^2}$. The normal vector to the body surface is denoted $\mathbf{n} = (n_1, n_2, n_3)$ and the additional notation $(n_4, n_5, n_6) = \mathbf{x} \times \mathbf{n}$ and $n_7 = -\partial \phi_0 / \partial \mathbf{n}$ is adopted. Using this notation, the boundary conditions on the solid surfaces are:

$$\frac{\partial \phi_j^{E,I}}{\partial \mathbf{n}} = n_j \quad \text{on } S_{E,I}, \quad j = 1, \dots, 7. \quad (9)$$

The flow through the porous wall in the normal direction is assumed to be continuous on either side of the boundary, so that

$$\frac{\partial \phi_j^E}{\partial \mathbf{n}} = \frac{\partial \phi_j^I}{\partial \mathbf{n}} \quad \text{on } S_P, j = 1, \dots, 7. \quad (10)$$

It is assumed that the pressure drop across the porous wall is proportional to a linear drag and inertia term. Under this assumption, the boundary condition on the porous wall can be written as (Sollitt & Cross, 1972; Yu, 1995)

$$\frac{\partial \phi_j^{E,I}}{\partial n} = n_j - ikG(\phi_j^E - \phi_j^I) \quad \text{on } S_P, j = 1, \dots, 7 \quad (11)$$

where G is the non-dimensional porous effect parameter and $\text{Re}(G)$ represents the linearised drag effect of the porous wall and $\text{Im}(G)$ represents the inertial effect. A value of $G = 0$ corresponds to a solid body and increasing G corresponds to increasing porosity (i.e. increasing size of perforations relative to the solid part). $G = \infty$ corresponds to the porous wall not being present (i.e. no resistance).

3 BEM SOLUTION

Application of Green's third identity to the domain bounded by the external body surfaces (S_E and S_P), the free surface, the sea bed and a control surface at infinity yields the following integral equation for the exterior domain (see e.g. Linton & McIver, 2001):

$$\begin{aligned} -2\pi\phi_j^E(\mathbf{P}) = \\ \int_{S_E \cup S_P} \left(\phi_j^E(\mathbf{Q}) \frac{\partial G(\mathbf{P}, \mathbf{Q})}{\partial n_Q} - G(\mathbf{P}, \mathbf{Q}) \frac{\partial \phi_j^E(\mathbf{Q})}{\partial n_Q} \right) dS, \quad (12) \\ j = 1, \dots, 7 \end{aligned}$$

where \mathbf{P} and \mathbf{Q} are points on the body surface and G is the wave Green function, defined below, which satisfies conditions (2)-(4) and (8). Note that the integrals over the free surface, sea bed and control surface vanish as a result of the conditions (3), (4) and (8). Similarly, application of Green's third identity to the domain bounded by the surfaces S_I , S_P and the free surface yields the following integral equation for the interior domain:

$$\begin{aligned} 2\pi\phi_j^I(\mathbf{P}) = \\ \int_{S_I \cup S_P} \left(\phi_j^I(\mathbf{Q}) \frac{\partial G(\mathbf{P}, \mathbf{Q})}{\partial n_Q} - G(\mathbf{P}, \mathbf{Q}) \frac{\partial \phi_j^I(\mathbf{Q})}{\partial n_Q} \right) dS, \quad (13) \\ j = 1, \dots, 7 \end{aligned}$$

Note that the opposite sign occurs on first term as the surface normal vectors are pointing into the fluid in the interior domain.

The Green function describes the wave potential at point $\mathbf{P} = (x, y, z)$ due to a pulsating wave source at point $\mathbf{Q} = (\xi, \eta, \zeta)$. In infinite depth, the Green function can be written as:

$$G(\mathbf{P}, \mathbf{Q}) = \frac{1}{r} + \frac{1}{r'} + \frac{2K}{\pi} \int_0^\infty \frac{\exp(v(z+\zeta))}{v-K} J_0(vr_0) dv \quad (14)$$

and in finite depth it can be written as:

$$\begin{aligned} G(\mathbf{P}, \mathbf{Q}) = \frac{1}{r} + \frac{1}{r''} + \\ 2 \int_0^\infty \frac{(v+K) \cosh(v(z+h)) \cosh(v(\zeta+h))}{v \sinh(vh) - K \cosh(vh)} e^{-vh} J_0(vr_0) dv, \quad (15) \end{aligned}$$

where $K = \omega^2/g$ is the infinite-depth wavenumber, J_0 is the zero order Bessel function of the first kind and

$$r = \{(x-\xi)^2 + (y-\eta)^2 + (z-\zeta)^2\}^{1/2}, \quad (16)$$

$$r' = \{(x-\xi)^2 + (y-\eta)^2 + (z+\zeta)^2\}^{1/2}, \quad (17)$$

$$r'' = \{(x-\xi)^2 + (y-\eta)^2 + (z+\zeta+2h)^2\}^{-1/2}, \quad (18)$$

$$r_0 = \{(x-\xi)^2 + (y-\eta)^2\}^{1/2}. \quad (19)$$

For the infinite depth case, the Green function has been computed using a look-up table method, based on the algorithms described by Newman (1985, 1992). In finite depth, when $r_0/h > 0.1$, the Green function is computed using the series method defined by John (1950) and when $r_0/h \leq 0.1$ the Green function is computed using the method described by Xie et al (2017).

The integral equations (14) and (15) are solved by discretising the body surface into a number of flat panels, with N_E panels on S_E , N_I panels on S_I and N_P panels on S_P . The panels on the porous surface are used for both the interior and exterior boundary integrals. The points $\mathbf{x}_i = (x_i, y_i, z_i)$, where the integral equations are enforced, are defined to be at the panel centroids. The panels are numbered with those on solid parts coming first, followed by the panels on the porous parts of the structure, so that $\boldsymbol{\phi}_j^{ES} = (\phi_j^E(\mathbf{x}_1), \dots, \phi_j^E(\mathbf{x}_{N_E}))^T$ are the potentials at the centroids of the solid panels of the exterior surface and $\boldsymbol{\phi}_j^{EP} = (\phi_j^E(\mathbf{x}_{N_E+1}), \dots, \phi_j^E(\mathbf{x}_{N_E+N_P}))^T$ are the potentials at the centroids of the exterior porous panels. Similarly, define $\boldsymbol{\phi}_j^{IS} = (\phi_j^I(\mathbf{x}_1), \dots, \phi_j^I(\mathbf{x}_{N_I}))^T$ and $\boldsymbol{\phi}_j^{IP} = (\phi_j^I(\mathbf{x}_{N_I+1}), \dots, \phi_j^I(\mathbf{x}_{N_I+N_P}))^T$ for the potentials on the solid and porous panels of interior surface.

Define coefficient matrices for the interior and exterior problems, \mathbf{D}^E , \mathbf{D}^I , \mathbf{S}^E , \mathbf{S}^I , as

$$D_{ik}^{E,I} = \begin{pmatrix} + \\ - \end{pmatrix} 2\pi\delta_{ik} + \int_{S_k} \frac{\partial G(\mathbf{x}_i, \mathbf{x}_k)}{\partial n_k} dS, \quad (20)$$

$$S_{ik}^{E,I} = \int_{S_k} G(\mathbf{x}_i, \mathbf{x}_k) dS, \quad (21)$$

where S_k is the surface of the k^{th} panel (of the exterior/interior problem respectively), δ_{ik} is the Kronecker delta function and the notation $\begin{pmatrix} + \\ - \end{pmatrix}$ indicates a plus for the matrix \mathbf{D}^E and a minus for the matrix \mathbf{D}^I . The integrals of the singular parts of the Green function and its derivative in (21) are computed using the algorithms of Newman (1986) and the irregular parts are assumed to be constant over each panel. The coefficient matrices can be written as block matrices:

$$\mathbf{D}^{E,I} = \begin{pmatrix} \mathbf{D}_{SS}^{E,I} & \mathbf{D}_{SP}^{E,I} \\ \mathbf{D}_{PS}^{E,I} & \mathbf{D}_{PP}^{E,I} \end{pmatrix}, \quad \mathbf{S}^{E,I} = \begin{pmatrix} \mathbf{S}_{SS}^{E,I} & \mathbf{S}_{SP}^{E,I} \\ \mathbf{S}_{PS}^{E,I} & \mathbf{S}_{PP}^{E,I} \end{pmatrix}, \quad (22)$$

where the submatrices $\mathbf{D}_{SS}^{E,I}$, $\mathbf{S}_{SS}^{E,I}$ and $\mathbf{D}_{PP}^{E,I}$, $\mathbf{S}_{PP}^{E,I}$ correspond to the terms between the solid and porous panels respectively and the other submatrices correspond to the remaining terms. If it is assumed that the potential is constant on each panel, then the integral equations (12) and (13) can then be written in discrete form:

$$\begin{pmatrix} \mathbf{D}_{SS}^E & \mathbf{D}_{SP}^E \\ \mathbf{D}_{PS}^E & \mathbf{D}_{PP}^E \end{pmatrix} \begin{pmatrix} \boldsymbol{\phi}_j^{ES} \\ \boldsymbol{\phi}_j^{EP} \end{pmatrix} = \begin{pmatrix} \mathbf{S}_{SS}^E & \mathbf{S}_{SP}^E \\ \mathbf{S}_{PS}^E & \mathbf{S}_{PP}^E \end{pmatrix} \begin{pmatrix} \mathbf{n}_j^{ES} \\ \mathbf{n}_j^{EP} \end{pmatrix} - ikG \begin{pmatrix} 0 \\ \boldsymbol{\phi}_j^{EP} - \boldsymbol{\phi}_j^{IP} \end{pmatrix}, \quad (23)$$

$$\begin{pmatrix} \mathbf{D}_{SS}^I & \mathbf{D}_{SP}^I \\ \mathbf{D}_{PS}^I & \mathbf{D}_{PP}^I \end{pmatrix} \begin{pmatrix} \boldsymbol{\phi}_j^{IS} \\ \boldsymbol{\phi}_j^{IP} \end{pmatrix} = \begin{pmatrix} \mathbf{S}_{SS}^I & \mathbf{S}_{SP}^I \\ \mathbf{S}_{PS}^I & \mathbf{S}_{PP}^I \end{pmatrix} \begin{pmatrix} \mathbf{n}_j^{IS} \\ \mathbf{n}_j^{IP} \end{pmatrix} - ikG \begin{pmatrix} 0 \\ \boldsymbol{\phi}_j^{EP} - \boldsymbol{\phi}_j^{IP} \end{pmatrix}, \quad (24)$$

where \mathbf{n}_j^{ES} , \mathbf{n}_j^{EP} , \mathbf{n}_j^{IS} and \mathbf{n}_j^{IP} are column vectors composed of the variables n_j corresponding to the panels of the solid/porous parts of the exterior/interior surfaces respectively. In the expressions above, the boundary conditions (9) has been applied on the solid panels and (11) has been applied on the porous panels. The expressions above assume a constant porosity coefficient G on all panels. However, a variable porosity could be accommodated by bringing the coefficient G inside the last column vector of (23) and (24). Collecting terms and combining these two systems of equations gives a single matrix equation that can be solved for the potentials in the interior and exterior domains:

$$\begin{pmatrix} \mathbf{D}_{SS}^E & \mathbf{D}_{SP}^E + ikG\mathbf{S}_{SP}^E & \mathbf{0} & -ikG\mathbf{S}_{SP}^E \\ \mathbf{D}_{PS}^E & \mathbf{D}_{PP}^E + ikG\mathbf{S}_{PP}^E & \mathbf{0} & -ikG\mathbf{S}_{PP}^E \\ \mathbf{0} & ikG\mathbf{S}_{SP}^I & \mathbf{D}_{SS}^I & \mathbf{D}_{SP}^I - ikG\mathbf{S}_{SP}^I \\ \mathbf{0} & ikG\mathbf{S}_{PP}^I & \mathbf{D}_{PS}^I & \mathbf{D}_{PP}^I - ikG\mathbf{S}_{PP}^I \end{pmatrix} \begin{pmatrix} \boldsymbol{\phi}_j^{ES} \\ \boldsymbol{\phi}_j^{EP} \\ \boldsymbol{\phi}_j^{IS} \\ \boldsymbol{\phi}_j^{IP} \end{pmatrix} = \begin{pmatrix} \mathbf{S}_{SS}^E & \mathbf{S}_{SP}^E & \mathbf{0} & \mathbf{0} \\ \mathbf{S}_{PS}^E & \mathbf{S}_{PP}^E & \mathbf{0} & \mathbf{0} \\ \mathbf{0} & \mathbf{0} & \mathbf{S}_{SS}^I & \mathbf{S}_{SP}^I \\ \mathbf{0} & \mathbf{0} & \mathbf{S}_{PS}^I & \mathbf{S}_{PP}^I \end{pmatrix} \begin{pmatrix} \mathbf{n}_j^{ES} \\ \mathbf{n}_j^{EP} \\ \mathbf{n}_j^{IS} \\ \mathbf{n}_j^{IP} \end{pmatrix}. \quad (25)$$

The formulation presented here can easily be extended to multiple bodies or single bodies with multiple unconnected porous domains. However, this is not considered further here.

Once the velocity potentials have been solved, the hydrodynamic forces can be evaluated in the normal way, by integrating the pressure over the interior and

exterior surfaces. The pressure is given by the linearised Bernoulli equation $p_j = -\rho\partial\phi_j/\partial t$. The excitation force (or moment) in the j^{th} mode is the sum of the force (or moment) on the internal and external surfaces:

$$F_j = \rho g A \left[\int_{S_E \cup S_P} (\phi_0^E + \phi_j^E) n_j dS - \int_{S_I \cup S_P} (\phi_0^I + \phi_j^I) n_j dS \right]. \quad (26)$$

Note that the surface normal vectors are pointing in the opposite direction in the interior domain so the force on the interior surfaces has the opposite sign in (26). The added mass, a_{ij} , and radiation damping coefficient, b_{ij} , are defined by:

$$a_{ij} - i \frac{b_{ij}}{\omega} = \rho \left[\int_{S_E \cup S_P} \phi_i^E n_j dS - \int_{S_I \cup S_P} \phi_i^I n_j dS \right], \quad i, j = 1, \dots, 6. \quad (27)$$

4 VERIFICATION

The BEM model described in Section 3 has been implemented in MATLAB. Variations on two canonical cases are considered for the verification of the BEM model – a floating hemisphere and a vertical circular cylinder. Results are presented first for the case of a solid hemisphere, followed by results for a porous hemisphere. For the vertical cylinder, we first consider a bottom-standing solid circular cylinder, then the same cylinder surrounded by a porous outer cylinder and finally a truncated cylinder with a porous upper wall and solid inner column (sketched in Figure 1).

4.1 Hemisphere

4.1.1 Solid hemisphere

For the case of the solid hemisphere in deep water the results from the BEM model have been verified against WAMIT version 6.4 (www.wamit.com). WAMIT has been run in low order mode (flat panels) with the option to remove “irregular frequencies” (discussed below) turned off. Running WAMIT in this way provides a numerically equivalent system, which will serve to verify whether the BEM model has been implemented correctly for the case of a solid body in deep water. A mesh convergence study was conducted in WAMIT and it was found that discretising the surface using an angular resolution of $\pi/20$ was sufficient to achieve stable estimates of the hydrodynamic coefficients. This resulted in a mesh with 351 panels, shown in Figure 2. Both WAMIT and the BEM model were run using the same mesh and same frequencies in the range $0 - 10 kR_0$, where R_0 is the radius.

The resulting non-dimensional surge and heave excitation forces, added mass and radiation damping from WAMIT and the BEM model are shown in Figure 3. The results from the two codes coincide exactly, indicating that the BEM model has been implemented correctly and the calculation of the deep water Green function is sufficiently precise. The results from both codes show the effects of “irregular frequencies”. These are frequencies at which the linear system becomes ill-conditioned and the results exhibit non-physical spikes. Methods exist to remove these effects for wave-interactions with solid bodies (see e.g. Lee & Scлавounos, 1989; Liu & Falzarano, 2017a, b). However, these methods have not yet been implemented in the BEM model and the extension to combined solid-porous structures will be considered in future work.

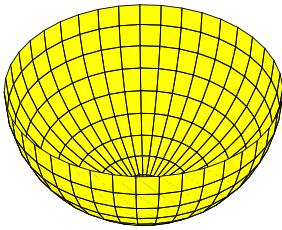


Figure 2. Mesh used in cases 1.1 and 1.2.

4.1.2 Porous hemisphere

The case of a porous hemisphere in deep water was considered by Dokken et al. (2017), who used a modified version of WAMIT version 5.3. Dokken et al. assume that the variable $\sigma = kG/\omega$ is constant in their porous boundary condition, rather than G . Zhao et al (2010) obtained a good match between numerical and experimental data for a truncated porous cylinder, by assuming that G is constant with frequency (but dependent on wave steepness). We have therefore opted to use this formulation in our porous boundary condition (11). However, for comparison with the results of Dokken et al., the BEM model has been run with σ constant. Under this assumption, the method presented in Section 3 is identical to that of Dokken et al. for the case of a fully porous structure, and should be expected to give equivalent results.

The BEM model was run using the same mesh as for the solid case. The nondimensional surge and heave excitation forces on the hemisphere are shown in Figure 4 and the nondimensional added mass and damping coefficients are shown in Figure 5. There is good agreement in the excitation forces between the BEM model and the modified WAMIT code. A reduction in excitation force with increasing porosity is evident. The surge force decreases to zero when $KR_0 = \pi/2$ ($R_0 = \lambda/4$), due to a resonance in the interior domain. This effect does not occur for the case of the solid hemisphere, shown in Figure 3.

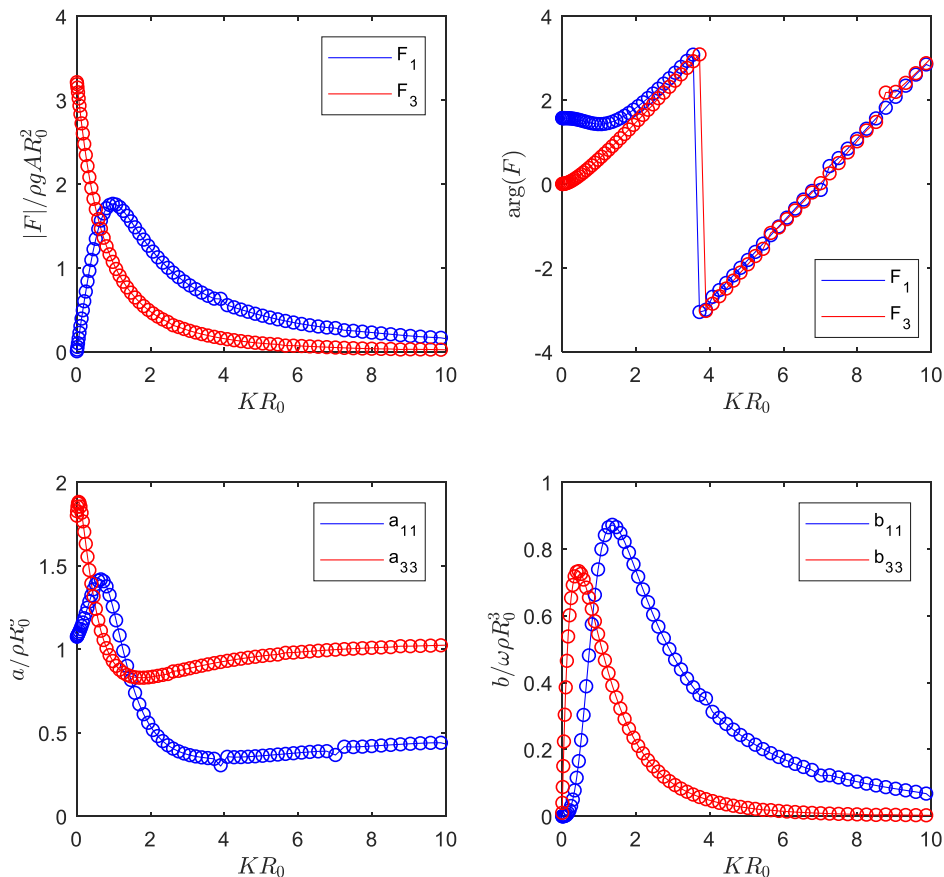


Figure 3. Comparison of dimensionless heave and surge excitation force, added mass and damping from BEM model (lines) and WAMIT (circles) for solid hemisphere in deep water.

Dokken et al. reported a_{11} , a_{33} , b_{11} and b_{33} for a range of values of σ , but did not present results for all combinations, so comparisons are shown in Figure 5 for the cases reported. The results are in good agreement for the cases considered. There is a significant variation in the added mass and damping coefficients with different values of σ , indicating that responses of floating structures could potentially be significantly altered through the addition of porous elements.

4.2 Cylinders

4.2.1 Solid vertical cylinder

For this case, the results from the BEM model are compared against an analytical solution for the surge excitation force on a bottom-standing vertical cylinder of radius a in water depth h . This is given in non-dimensional form as (Mei, 1983):

$$\frac{F_x}{\rho g A a h} = \frac{4}{ka H_1'(ka)} \frac{\tanh(kh)}{kh}, \quad (28)$$

where H_1 is the first-order Hankel function of the first kind and the prime denotes the derivative with respect to the arguments. In the case considered, $a = h/2$. The mesh used has been discretised using 40 panels around the circumference and 20 in the vertical and radial directions, giving a total of 1200 panels. The results are shown in Figure 6. The numerical and analytical results are in good agreement throughout the

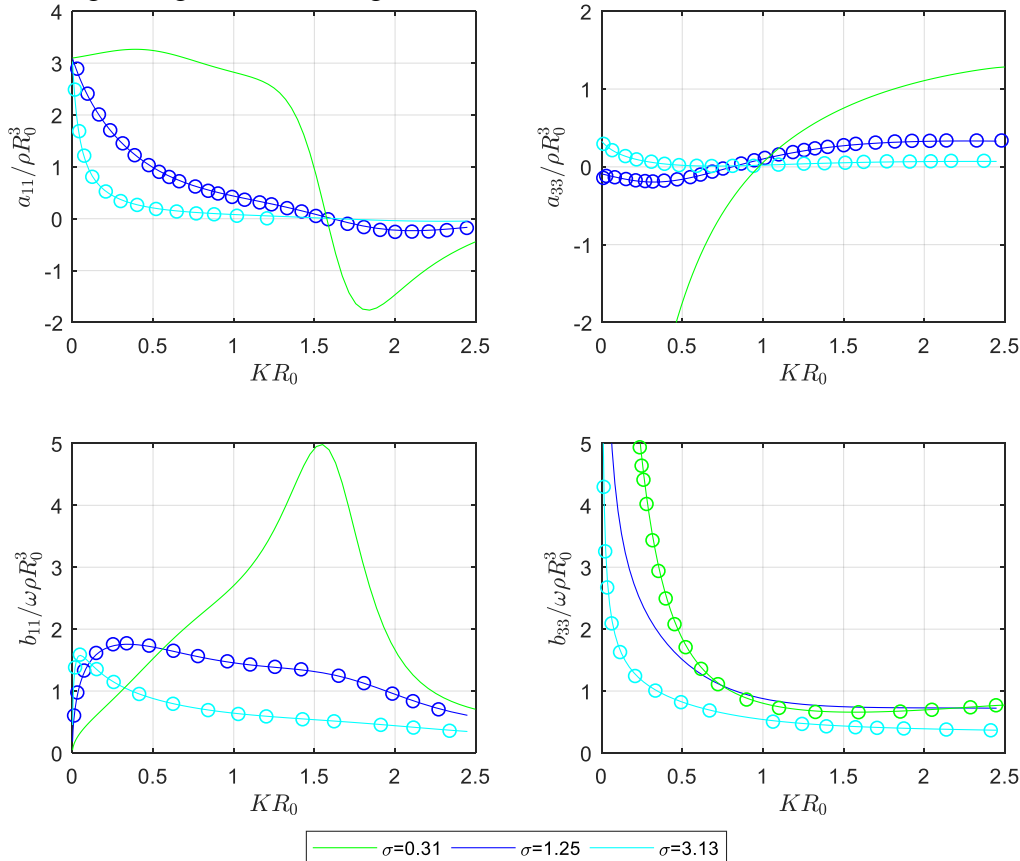


Figure 5. Nondimensional added mass and damping coefficients for a floating porous hemisphere for three values of porosity coefficient σ . Solid lines are results from BEM model. Circles are results reported by Dokken et al. (2017).

range, although a small dip in the BEM results at $ka \approx 3.9$ is visible, which is a result of an irregular frequency (this has been verified through comparison to results from WAMIT, not shown here).

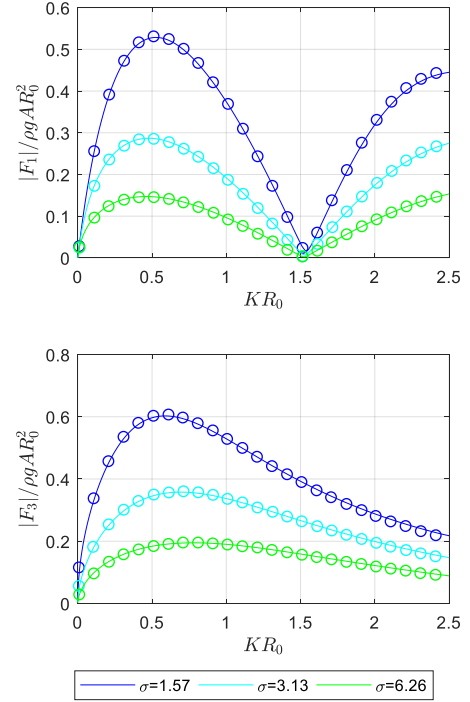


Figure 4. Nondimensional heave and surge excitation forces on a floating porous hemisphere for three values of porosity coefficient σ . Solid lines are results from BEM model. Circles are results reported by Dokken et al. (2017).

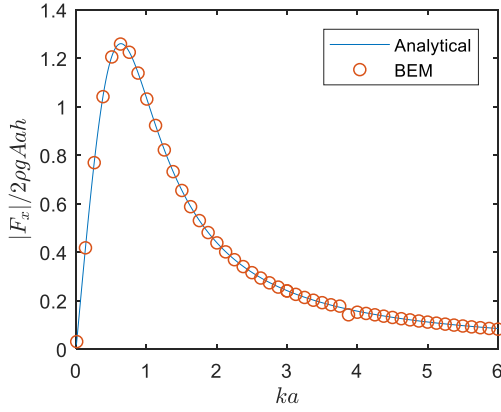


Figure 6. Comparison of normalised surge excitation force on a bottom-standing vertical circular cylinder of radius $a = h/2$ from BEM model and analytical solution

4.2.2 Concentric porous cylinder

The second case considered consists of a solid bottom-standing vertical cylinder with a concentric porous outer cylinder. An analytical solution for this case was presented by Wang & Ren (1994) and will be used for verification of the BEM model. Due to space restrictions, the analytical solution is not repeated here and the reader is referred to the original paper for details. In the case considered, the inner cylinder has radius $a = h/2$ and the outer cylinder has radius $b = 2a$ and the porosity coefficient is set as $G = 2$. The mesh used in this example is shown in Figure 7 and has a vertical and radial resolution of 8 panels and 40 panels around the circumference. This results in a total of 624 panels for the external domain and 780 panels for the internal domain.

The normalised surge excitation force on the inner and outer cylinders is shown in Figure 8. There is generally good agreement between the BEM and analytical models, although the BEM model predicts a marginally lower second peak in the force on the outer cylinder. The force on the outer cylinder goes to zero for $ka \approx 0.68$. There is no simple expression for the frequency at which the force on the outer cylinder goes to zero. This frequency is a function of the ratios between a , b and G (see Wang & Ren, 1994, for details). The combined force on the inner and outer cylinders is shown in Figure 9. Again, there is good agreement between the BEM and analytical results (as implied by the results in Figure 8). The normalised force on the inner cylinder, without the outer cylinder present, is also shown. The inclusion of the porous outer cylinder leads to a reduction in the total force for frequencies above the peak response, but an increase in force at lower frequencies.

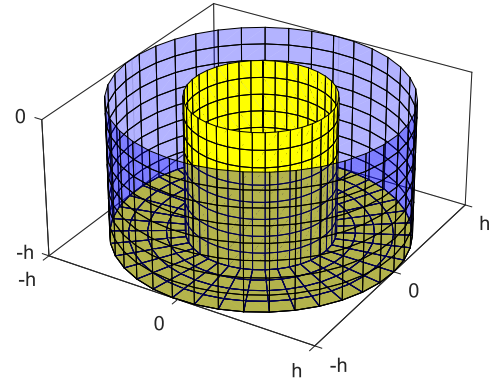


Figure 7. Mesh used for case 2.2. Solid panels are shown in yellow and porous panels are shown in translucent blue.

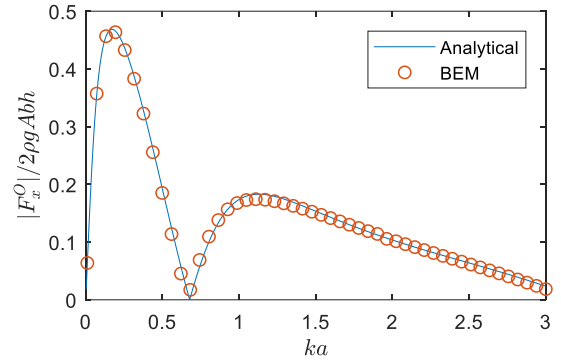
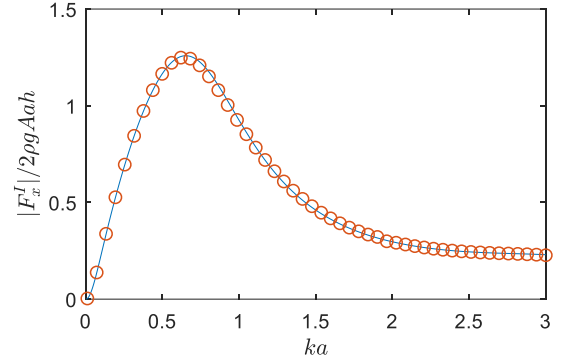


Figure 8. Normalised surge excitation forces on inner and outer cylinder from analytical and BEM models for concentric porous cylinders with $G = 2$, $a = h/2$ and $b = 2a$.

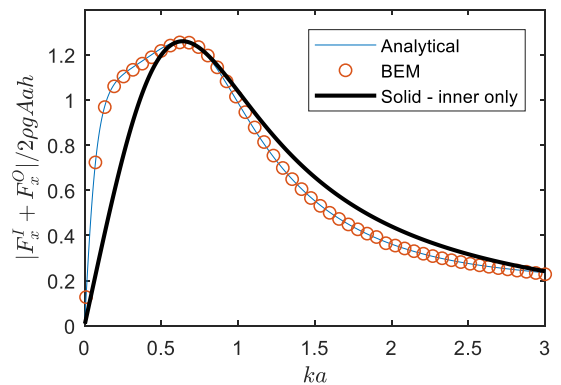


Figure 9. Total normalised surge excitation forces on concentric porous cylinders from analytical and BEM models for case shown in Figure 9. Analytical result for inner cylinder only is shown for comparison.

4.2.3 Truncated porous cylinder

The final case considered is a truncated cylinder with a porous upper sidewall and solid inner column.

An analytical solution for this case was presented by Ning et al. (2017). In the example presented, the inner cylinder has radius $a = h/3$ and the outer cylinder has radius $b = 2a$. The draft of the structure is $d = b$ and the draft of the porous upper wall is $d_p = d/2$. The mesh used for the BEM model is illustrated in Figure 10 and has 780 panels on the external surfaces and 585 on the internal surfaces.

Figure 11 shows the dimensionless surge and heave excitation forces from the BEM and analytical models for the cases $G = 0.5 - 0.5i$ and $G = 1 - 1i$ (note that this is the complex conjugate of the values of G reported by Ning et al. (2017), as they have used a time dependency of $e^{-i\omega t}$ rather than $e^{i\omega t}$ in our case). The surge excitation forces are in good agreement with the results of Ning et al. However, the heave excitation forces show a clear influence of an irregular frequency in the BEM model at $kb \approx 2.5$, which causes a discrepancy with the analytical result. Despite this, the general trends in the heave forces are replicated. Removal of irregular frequency effects will be considered in future work.

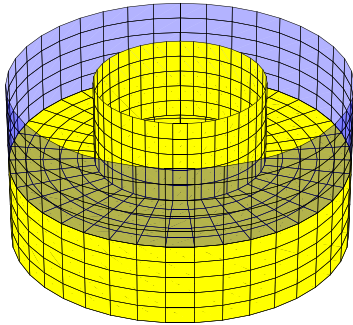


Figure 10. Mesh used for case 2.3 - truncated cylinder with porous upper sidewall and solid inner column.

5 CONCLUSIONS AND FUTURE WORK

A method has been presented for calculating wave forces on structures with solid and porous elements of arbitrary shape. Initial verification results for the new method have been presented using commercial BEM software as reference for solid bodies and published analytical and numerical results for porous/solid structures for some simple geometries. The comparisons against the reference data showed good agreement in all cases, indicating that the method can be used with confidence in more complex cases where analytical results cannot be derived.

The BEM model described here will be used to study the load and response characteristics of floating offshore wind platforms with porous elements for various configurations (spar, semi-submersible and tension leg platform).

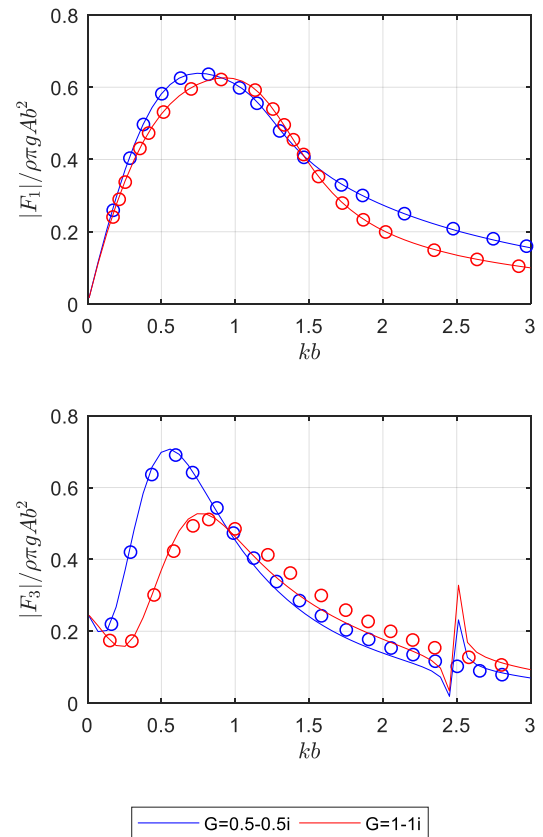


Figure 11. Comparison of dimensionless surge and heave excitation forces on truncated cylinder with porous upper side wall from BEM (lines) and analytical models (circles).

ACKNOWLEDGEMENT

This work was funded through EPSRC grant EP/R007519/1 for the project ‘‘Resilient Integrated-Coupled Floating Offshore Wind Platform Design Methodology (ResIn)’’.

REFERENCES

- Cho IH, Kim MH. Wave absorbing system using inclined perforated plates. *J Fluid Mech* 2008;608:1–20.
- Crowley S, Porter R, 2012. An analysis of screen arrangements for a tuned liquid damper. *J. Fluids and Structures* 34, 291–309
- Dokken J, Grue J, Karstensen LP, 2017. Wave analysis of porous geometry with linear resistance law. *J. Marine Science and Application*, 16, 1–10
- Downie MJ, Wang J, Graham JMR, 2000. The Effectiveness of Porous Damping Devices. *Proc 10th International Offshore and Polar Engineering Conference*, 28 May-2 June, Seattle, Washington, USA
- Faltinsen OM, Firoozkoobi R, Timokha AN, 2011. Steady-state liquid sloshing in a rectangular tank with a slat-type screen in the middle: Quasilinear modal analysis and experiments. *Physics of Fluids* 23, 042101
- Feng XY, Chen XB, Liang H, Dias F, 2017. Analysis of dissipation on gap resonance between side-by-side barges. *10th International Workshop on Ship and*

Marine Hydrodynamics, Keelung, Taiwan, November 5-8, 2017

Huang ZH, Li YC, Liu Y. Hydraulic performance and wave loadings of perforated/slotted coastal structures: a review. *Ocean Eng* 2011;38(10):1031–53.

Ijima T, Chou CR, Yoshida A, 1976. Method of analyses for two-dimensional water wave problems. *Proc. Conf. Coastal Eng.*, Honolulu, HI, pp. 2717–2736.

John F, 1950. On the motion of floating bodies II. *Comm. Pure Appl. Math.* 3, 45–101.

Lee CH, Sclavounos PD, 1989. Removing the irregular frequencies from integral equations in wave-body interactions. *J. Fluid Mech.* 207, 393.

Lee CP, Ker WK, 2002. Coupling of linear waves and a hybrid porous TLP. *Ocean Eng.* 29 (9), 1049–1066.

Linton CM, McIver P, 2001. *Handbook of mathematical techniques for wave/structure interactions*. Chapman and Hall.

Liu Y, Falzarano JM, 2017a. Irregular frequency removal methods: theory and applications in hydrodynamics. *J Mar Syst Ocean Technol*, 12:49–64.

Liu Y, Falzarano JM, 2017b. A method to remove irregular frequencies and log singularity evaluation in wave-body interaction problems. *J. Ocean Eng. Mar. Energy* (2017) 3:161–189

Liu Y, Li HJ, Li YC, 2012. A new analytical solution for wave scattering by a submerged horizontal porous plate with finite thickness. *Ocean Eng*, 42:83–92.

Liu Y, Li H, 2017. Iterative multi-domain BEM solution for water wave reflection by perforated caisson breakwaters. *Engineering Analysis with Boundary Elements*, 77, 70–80

Mallayachari V, Sundar V, 1994. Reflection characteristics of permeable seawalls. *Coast. Eng.*, 23(1–2):135–50.

Mei CC, 1983. *The Applied Dynamics of Ocean Surface Waves*. World Scientific. Advanced Series on Ocean Engineering: Volume 1.

Molin B, 2011. Hydrodynamic modeling of perforated structures. *Appl. Ocean Res.*, 2011, 33:1–11

Molin B, Remy F, 2013. Experimental and numerical study of the sloshing motion in a rectangular tank with a perforated screen. *J Fluid Struct* 43, 463–480

Molin B, Remy F, 2015. Inertia effects in TLD sloshing with perforated screens. *J Fluid Struct* 2015; 59:165–77

Newman JN, 1985. Algorithms for the Free-Surface Green Function. *J. Eng. Math.*, 19, 57–67

Newman JN, 1986. Distribution of Sources and Dipoles over a Quadrilateral. *J. Eng. Math*, 20, 113–126.

Newman JN, 1992. The approximation of free-surface Green functions. *Wave Asymptotics*, PA Martin & GR Wickham, editors, Cambridge University Press. ISBN:9780521414142

Ning D, Zhao X, Teng B, Johanning L, 2017. Wave diffraction from a truncated cylinder with an upper porous sidewall and an inner column. *Ocean Eng.*, 130, 471–481

Park MS, Jeong YJ, You YJ, Lee DH, Kim HC, 2014. Numerical analysis of a gravity substructure with partial porous area for offshore wind turbines. *J. Civ. Eng. Archit. Res.* 1 (4), 230–238.

Sollitt CK, Cross RH, 1972. Wave transformation through permeable breakwaters. *Proc. 13th Int. Conf. on Coastal Eng.*, pp.1827–1846

Sulisz W, 1985. Wave reflection and transmission at permeable breakwater of arbitrary cross-section. *Coastal Eng.*, 9, 371–386

Wang KH, Ren X, 1994. Wave interaction with a concentric porous cylinder system. *Ocean Eng.* 21(4):343–360.

Williams AN, Li W, 1998. Wave interaction with a semi-porous cylindrical breakwater mounted on a storage tank. *Ocean Eng.* 25(2–3):195–219

Williams AN, Li W, 2000. Water wave interaction with an array of bottom mounted surface-piercing porous cylinders. *Ocean Eng.* 27(8):841–866

Williams AN, Li W, Wang K-H, 2000. Water wave interaction with a floating porous cylinder. *Ocean Eng.* 27(1):1–28

Xie Z, Liu Y, Falzarano J, 2017. A more efficient numerical evaluation of the green function in finite water depth. *Ocean Sys. Eng.*, 7, 4, 399–412.

Yu, X. 1995. Diffraction of water waves by porous breakwaters. *J. Waterway Port Coastal Ocean Eng.*, 121(6), 275–282.

Zhao F, Bao W, Kinoshita T, Itakura H, 2010. Theoretical and Experimental Study on a Porous Cylinder Floating in Waves. *J. Offshore Mech. Arct. Eng.* 2010;133(1):011301–011301–10